photonics

MDPI

Article

Adjacent In-Plane Air Referencing for Quantitative Complex Refractive-Index Mapping in Reflection THz Imaging

Lan-Hee Yang [1,†], Inhee Maeng [1,†], Young Bin Ji [2], Hyeon Sang Bark [2], Hee Jun Shin [3], Eui Su Lee [4], Seung Jae Oh [1,*] and Han-Cheol Ryu [5,*]

[1] YUHS-KRIBB Medical Convergence Research Institute, College of Medicine, Yonsei University, Seoul 03722, Republic of Korea; yangd5d5@yuhs.ac (L.-H.Y.); inheem@yuhs.ac (I.M.)
[2] Division of Applied Photonics System Research, Advanced Photonics Research Institute (APRI), Gwangju Institute of Science and Technology (GIST), Gwangju 61005, Republic of Korea; ybji.thz@gist.ac.kr (Y.B.J.); hyeonsang.bark@gist.ac.kr (H.S.B.)
[3] Pohang Accelerator Laboratory, Pohang University of Science and Technology (POSTECH), Pohang 37673, Republic of Korea; shinhj@postech.ac.kr
[4] Electronics and Telecommunications Research Institute, Daejeon 34129, Republic of Korea; euisu@etri.re.kr
[5] Department of Artificial Intelligence Convergence, Sahmyook University, Seoul 01795, Republic of Korea
* Correspondence: issac@yuhs.ac (S.J.O.); hcryu@syu.ac.kr (H.-C.R.)
† These authors contributed equally to this work.

Abstract

Quantitative terahertz (THz) reflection imaging requires a complex-field reference with a stable phase relationship to the specimen. A metal reflector measured in place of the sample, or an axially displaced window interface, can introduce systematic errors in tightly focused imaging. Here, an empty chamber on a quartz window serves as an adjacent in-plane air reference for three liquid-filled chambers. At each pixel, the quartz–sample field is divided by the quartz–air field recorded in the same scan and focal plane, and the known quartz–air Fresnel coefficient converts this ratio into the complex refractive index. For water and sucrose solutions at 30 and 60 wt%, the reflection-derived refractive index, absorption coefficient, and permittivity agreed with transmission measurements over 0.5–1.5 THz, with root-mean-square relative differences of 2.4–3.4%, 5.9–8.9%, and 5.0–9.2%, respectively. At 1.0 THz, the permittivity loss term decreased from 2.37 for water to 1.96 and 1.21 for the 30 and 60 wt% solutions, whereas the real permittivity remained between 3.95 and 4.44. In a double-Debye fit, the slow-relaxation contribution at 60 wt% was below the dilution estimate. Maps of these quantities were obtained from a single reflection image, and the surrounding bare quartz–air area served as an internal check of the reference.

Keywords: terahertz time-domain spectroscopy; reflection imaging; adjacent in-plane air reference; quartz; complex refractive index; sucrose solution; dielectric permittivity

Check for updates

Received: 29 September 2026
Revised: 25 October 2026
Accepted: 29 October 2026
Published: 30 October 2026

Copyright: © 2026 by the authors. Licensee MDPI, Basel, Switzerland. This article is an open access article distributed under the terms and conditions of the Creative Commons Attribution (CC BY) license.

1. Introduction

Terahertz (THz) radiation, with frequencies of approximately 0.1–10 THz, is used as a noncontact and nondestructive probe for material characterization and imaging [1]. Its sensitivity to polar molecules, low-energy intermolecular interactions, lattice vibrations, and free-carrier dynamics yields information that is difficult to obtain from conventional optical images alone. THz time-domain spectroscopy (THz-TDS) coherently measures both the amplitude and phase of the electric field. The measurement gives the frequency-dependent complex refractive index of a material, from which the absorption coefficient, dielectric permittivity, and electrical conductivity can be derived. THz-TDS has been applied to

semiconductor characterization, pharmaceutical analysis, food inspection, and biomedical imaging.

Transmission-mode THz-TDS is widely used because of its relatively straightforward optical configuration and data analysis, but its applicability is limited when absorption, electrical conductivity, or interfacial reflection substantially attenuates the transmitted field [2]. Liquid water absorbs THz radiation strongly, so aqueous specimens and water-rich biological tissues can be difficult to measure in transmission. The same may hold for conductive semiconductors, materials with a high refractive index or permittivity, and two-dimensional materials on THz-opaque substrates [3]. The transmitted field may then approach the dynamic-range limit of the measurement system or be blocked by the substrate. Reflection-mode THz-TDS probes a material's response at an accessible interface without requiring the THz field to propagate through the full sample thickness.

Some samples are also small in area or volume. Halide perovskites show strong THz features related to phonons and defects [4], but their single crystals may have little usable area. Exfoliated two-dimensional materials and patterned semiconductor structures may be similarly small. In a microfluidic flow chip, the THz beam must be concentrated within the liquid-filled channel to probe a small volume, and contributions from the surrounding channel structure and substrate must be kept low. Optics with a high numerical aperture (NA) reduce the lateral beam size and limit averaging over adjacent materials. Tight focusing therefore benefits THz microspectroscopy and the imaging of small or heterogeneous specimens. However, it also shortens the depth of focus, so quantitative measurements become more sensitive to an axial offset between the planes from which the reference and sample signals originate.

Reflection contrast does not by itself give the optical constants of a material. THz reflection images are often presented as peak-to-peak amplitude, reflectance, or normalized intensity maps. Their values depend on the optical alignment, the substrate, and the reference, not only on the sample. Quantitative retrieval of the complex refractive index generally requires a complex-field reference that preserves both amplitude and phase. Conventionally, a metallic reflector is placed at the nominal sample position and measured separately. Replacing the sample with the reflector can introduce a small axial position mismatch, and the resulting frequency-dependent phase error propagates into the retrieved optical constants [5–7]. Drift in the THz output or in other system conditions between the two measurements can add a further error to the ratio of the two signals. Reflection measurements with a fiber-coupled THz endoscope have yielded the refractive index and absorption of oral tissues and water [8].

Rather than a separately measured metallic reflector, the reflections from the two faces of a dielectric sample window can be used for self-referencing [9,10]. The pulses reflected from the air–window and window–sample interfaces are separated in time, and the propagation delay and Fresnel coefficients can be included in an analytical model. However, these reflections originate from different axial planes. In a tightly focused system, beam size, wavefront curvature, Gouy phase, and collection efficiency may vary between those planes. Propagation through a thick window can also change the focal conditions across the measured frequency band. If only the propagation delay is corrected, amplitude or phase differences may remain in the complex-field ratio. The magnitude of these effects depends on the optical arrangement and must be evaluated for the measurement system in use [11].

The reflection from a window–air interface is an established reference in reflection THz-TDS. Jepsen et al. used the reflection from the front surface of a silicon window as an internal reference for the sample reflection at its back surface and calibrated the system once with air behind the window [2]. Huang et al. improved the retrieval of optical constants by correcting for unwanted quartz-window reflections [12], and Chen et al. used

spatially corrected baseline and air-reference signals to obtain refractive-index and absorption maps [13]. In these studies, however, the calibration or air-reference measurement was made separately from the sample measurement, before the sample was loaded or in a separate scan. In continuous-wave solid-immersion THz microscopy, Chernomyrdin et al. normalized the backscattered intensity to that measured with air at the lens and reconstructed refractive-index maps with subwavelength resolution by fitting an analytical model [14]. With intensity data at a single frequency, the reconstruction for lossy samples such as tissues required an assumed relation between refractive index and absorption. THz-attenuated total reflection (ATR) spectroscopy compares the signal reflected at a prism–liquid interface with a reference signal. It is suited to highly absorbing liquids but remains sensitive to the optical alignment and to the reproducibility of the sample–prism contact [15]. Lordon et al. placed a sample and a water reference in adjacent wells on the same prism surface and probed them with the two halves of a THz beam [16]. One half was delayed, so both signals were recorded in a single waveform. Normalizing one signal by the other improved the long-term stability and increased the signal-to-noise ratio of the measured power about fivefold. The two halves of the beam followed different paths, which required a calibration with water in both wells, and the result was the reflection coefficient of the solution relative to that of water. THz time-domain ellipsometry takes the reference from the sample itself: the complex refractive index of a liquid follows from the amplitude ratio and phase difference of the s- and p-polarized components reflected from its surface at oblique incidence [17,18].

In the present approach, the quartz–air reflection in an empty chamber beside liquid-filled chambers is recorded in the same scan as the samples and used as the complex-field reference. The reference and sample regions share one quartz surface, and their reflections originate at the same nominal focal plane and pass through nominally the same thickness of quartz. The focusing and collection conditions should therefore be closely matched. Earlier reflection modeling and quartz-window imaging studies have shown how the window response and the refractive-index mismatch affect THz contrast [19,20]. Multiplying the measured sample-to-reference field ratio by the known quartz–air Fresnel reflection coefficient gives the quartz–sample reflection coefficient. Analytical inversion then yields the sample's complex refractive index at each pixel and frequency, from which the absorption coefficient and complex dielectric permittivity can be calculated. The accuracy of the retrieval depends on a uniform quartz window and a stable optical response across the scanned area. As in the two-well ATR scheme [16], the reference and the samples lie on one surface. Here, the reference is air rather than water, and a single focused beam probes them at different times during the scan rather than through two beam paths in one waveform. Drift during the scan therefore does not cancel, but its effect shows up in the bare quartz–air area that every scan line crosses (Section 4).

In this paper, we implement adjacent in-plane air referencing on a quartz window in a pulsed reflection imaging system with a nominal NA of 0.64. The reference is a region of the image itself, so the target does not have to be exchanged or remounted between the reference and sample measurements. The retrieval is tested on a four-region target containing an air reference, water, and sucrose solutions at 30 and 60 wt%. The reflection-derived spectra are compared quantitatively with independent transmission measurements and with the literature data for water, and the permittivity of the three liquids is described with a double-Debye model. We estimate the errors caused by oblique rays in the focused beam and by offsets of the reference plane, and we use the bare quartz–air area of the same image to check the reference and to locate scan-related errors in the maps. Finally, we compare peak-to-peak and spectral-amplitude maps with maps of the refractive index, absorption coefficient, and complex dielectric permittivity.

2. Materials and Methods

2.1. Samples and Quartz Window

Sucrose (≥99.5%, Sigma-Aldrich, St. Louis, MO, USA) was dissolved in distilled water to prepare aqueous sucrose solutions at concentrations of 30 and 60 wt%. A CoverWell™ eight-chamber perfusion chamber (PC8R-0.5, Grace Bio-Labs, Bend, OR, USA), consisting of a 0.6 mm thick silicone gasket with chambers 9 mm in diameter, was cut in half, and the resulting four-chamber section was attached to a quartz window. One chamber was left empty to provide a quartz–air reference on the same window and at the same nominal focal plane as the samples (Figure 1). The other three chambers contained distilled water, 30 wt% sucrose solution, and 60 wt% sucrose solution. The quartz window was z-cut and approximately 3 mm thick. Because the optic axis of a z-cut window is parallel to the propagation direction at normal incidence, the THz field experiences the ordinary refractive index of crystalline quartz. For the reflection inversion, we therefore used a frequency-independent complex quartz index, $N_q = 2.11 - 2.38 \times 10^{-4}\, i$, with the convention $N = n - i\kappa$. The real part of N_q is the ordinary index, which varies by less than 0.01 between 0.2 and 2 THz, and the imaginary part corresponds to a power absorption coefficient of approximately 0.1 cm^{-1} at 1 THz [21].

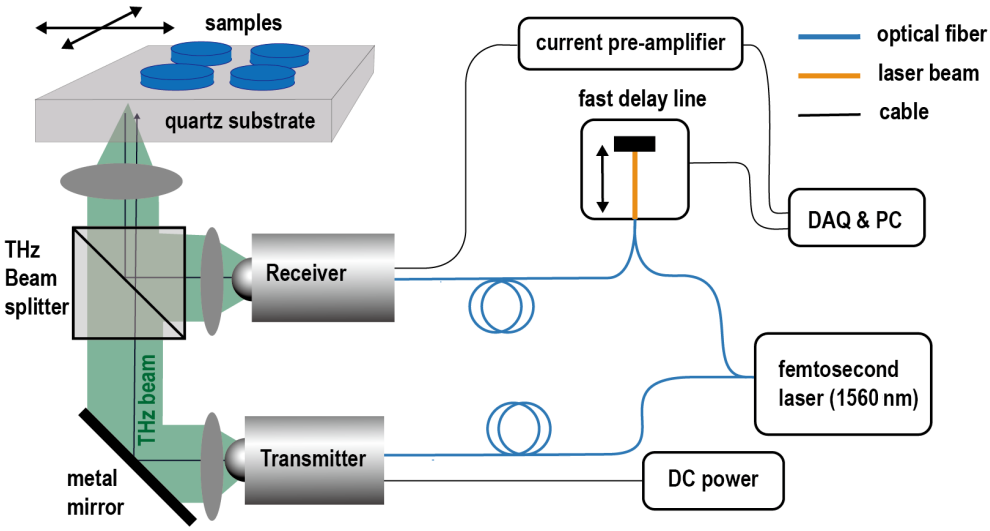


Figure 1. Schematic of the normal-incidence reflection terahertz (THz) imaging system and quartz-window target. A four-chamber section cut from an eight-chamber CoverWell™ perfusion chamber was attached to the quartz window. One chamber, left empty, provided the in-plane quartz–air reference.

2.2. Reflection-Mode THz Spectroscopy and Imaging

The reflection setup was based on previously reported THz imaging systems that use a silicon beam splitter and focus the THz beam onto the sample interface [20,22]. A 1560 nm femtosecond fiber laser drove the THz emitter and receiver. The emitted THz pulse passed through the beam splitter and was focused onto the sample side of the quartz window. The beam splitter directed the pulse reflected at the interface to the receiver. The focusing lens was an aspheric polymethylpentene (TPX) lens (LTA-D25.4-F10, BATOP, Jena, Germany) with a diameter of 25.4 mm, a clear aperture of 20 mm, a focal length of 10 mm, and an NA of 0.64 (half-angle 39.9°, manufacturer's specification). For this NA, the diffraction-limited spot diameter (full width at half maximum, $0.51\lambda/\mathrm{NA}$) is approximately 0.48 mm at 0.5 THz and 0.24 mm at 1.0 THz. A knife-edge scan across the focus in one lateral direction, in 50 μm steps, gave a line-spread function (the derivative of the peak-to-peak signal with respect to the edge position) with a full width at half maximum of 0.42 mm in a Gaussian

fit, and an error-function fit to the edge response gave 0.49 mm (10–90% edge widths of 0.45 and 0.54 mm). These widths refer to the broadband peak-to-peak signal rather than to a single frequency and are close to the diffraction-limited value at 0.5 THz. Waveforms were acquired with a fast optical delay line at a rate of 20 Hz over a 48 ps delay range, and the detector signal was amplified and digitized. The analyzed pulse in each waveform, near the middle of the 48 ps record (Figure 2c), is the reflection from the quartz–sample (or quartz–air) interface at the back of the window. The reflection from the front air–quartz surface precedes it by approximately 42 ps, the round-trip delay in 3 mm of quartz with an index of 2.11, and the first multiple reflection inside the window follows it by the same delay. Both lie outside the recorded range. The reflection module was housed in an acrylic enclosure kept at a relative humidity below 1%, and measurements were performed at 22 °C. A nominal 40 × 30 mm^2 area was raster scanned bidirectionally (adjacent lines in opposite directions) in 0.25 mm steps, giving 162 × 121 pixels. At this step size, a 9 × 9-pixel region of interest (ROI; 81 scan points) covers a nominal area of 2.25 × 2.25 mm^2.

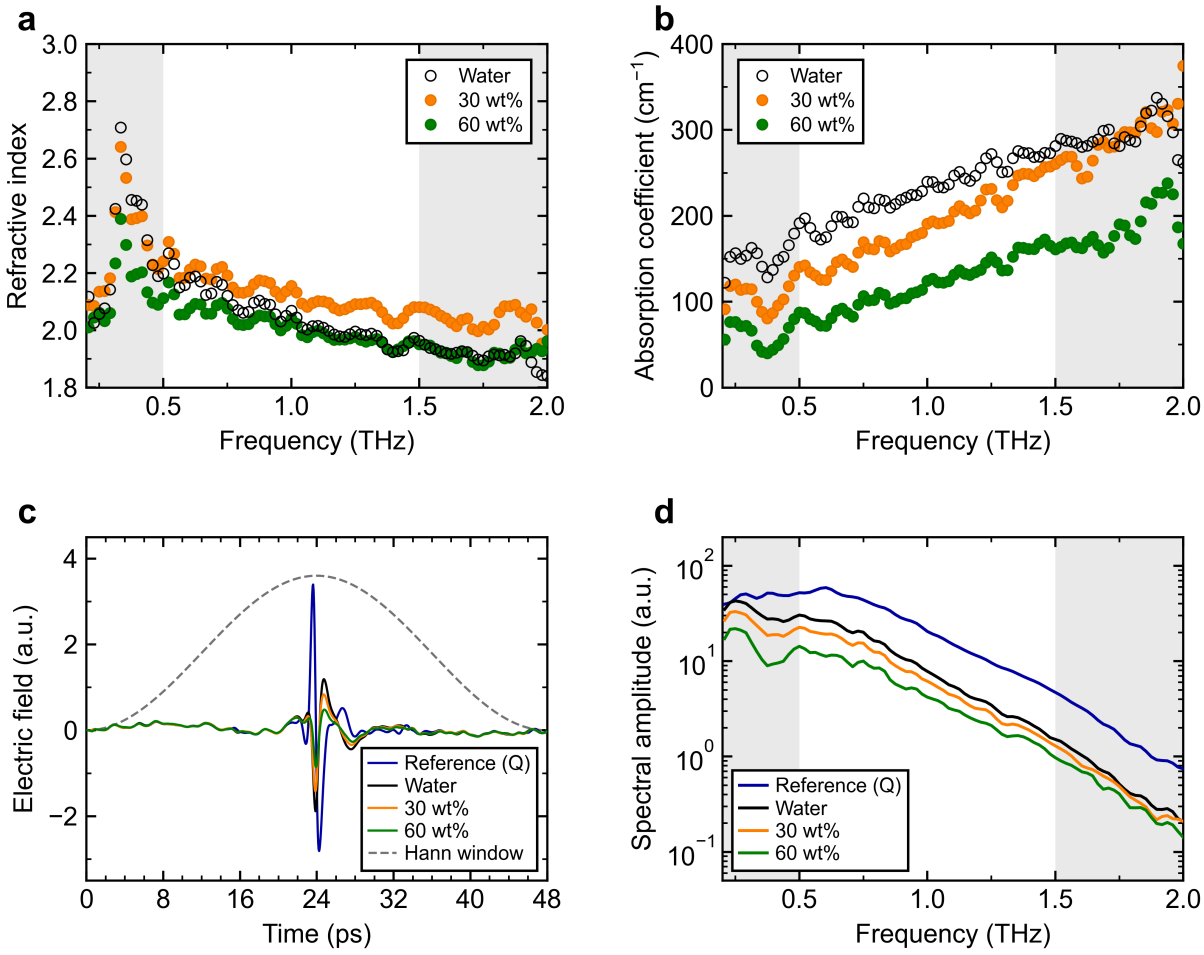


Figure 2. Reflection-derived (**a**) real refractive index and (**b**) power absorption coefficient of water and sucrose solutions at 30 and 60 wt%; (**c**) reflected waveforms (before windowing) of the quartz–air reference (Q) and the three liquids, each averaged over its region of interest (ROI), and the Hann window applied to all of them (dashed line, scaled); (**d**) amplitude spectra of the windowed waveforms. Markers in (**a**,**b**) show the mean of the 81 pixels in each 9 × 9-pixel sample ROI (nominal area 2.25 × 2.25 mm^2 at a 0.25 mm scan step); error bars for these data are shown in Section 3.3. Shaded areas lie outside the 0.5–1.5 THz band used for quantitative comparison.

2.3. Transmission-Mode THz Spectroscopy

Transmission-mode THz-TDS was carried out with a pump–probe system based on photoconductive THz generation and detection, similar to that described previously [22]. The system was driven by an approximately 780 nm, 85 fs, 100 MHz laser. A 130 V bias pulse modulated at 1.2 kHz was applied to the THz emitter, and the detected signal was demodulated using a lock-in amplifier. Two parabolic mirrors and two TPX lenses with a nominal focal length of 100 mm focused the THz beam onto a liquid cell consisting of two quartz windows separated by an approximately 184 μm spacer. THz time-domain waveforms were acquired by pump–probe sampling with a slow linear optical delay stage advanced in 5 μm increments. Transmission measurements were performed at 22 °C with the relative humidity below 1%.

A reference waveform was acquired through the empty liquid cell and a sample waveform through the same cell filled with each liquid, and both were Fourier transformed. The real refractive index and absorption coefficient were obtained by fitting the complex sample-to-reference ratio to a Fresnel-based quartz–liquid–quartz transmission model that includes interfacial transmission and coherent Fabry–Pérot multiple reflections within the thin liquid layer. The complex refractive index and dielectric permittivity were then calculated from the fitted values.

2.4. In-Plane Reference and Complex Fresnel Inversion

We adopt the complex-index convention $N_s(f) = n_s(f) - i\kappa_s(f)$, where n_s is the real refractive index and κ_s the extinction coefficient of the sample, with $\kappa_s \geq 0$ for a passive sample. For normal incidence from quartz into air or the sample, the complex field reflection coefficients are given by

$$r_{qa}(f) = \frac{N_q(f) - 1}{N_q(f) + 1}, \qquad r_{qs}(f) = \frac{N_q(f) - N_s(f)}{N_q(f) + N_s(f)} \tag{1}$$

The quartz–air reference and quartz–sample waveforms, $E_{qa}(t)$ and $E_s(t)$, were multiplied by the same Hann window, which spans the full 48 ps record (Figure 2c), and Fourier transformed on their original time axes, without any time shift or peak alignment. This preserved their relative timing and thus the phase of their ratio. If the system response is nearly the same at both positions and acquisition times, the measured complex-field ratio is

$$\rho(f) = \frac{E_s(f)}{E_{qa}(f)} \simeq \frac{r_{qs}(f)}{r_{qa}(f)} \tag{2}$$

Consequently, $r_{qs} = \rho(f)\, r_{qa}$, and the sample refractive index can be retrieved analytically as

$$N_s(f) = N_q(f)\, \frac{1 - \rho(f)\, r_{qa}(f)}{1 + \rho(f)\, r_{qa}(f)} \tag{3}$$

The absorption coefficient α, real permittivity ε_1, and positive dielectric-loss term ε_2 follow from

$$\alpha(f) = \frac{4\pi f \kappa_s(f)}{c}, \qquad \varepsilon_1 = n_s^2 - \kappa_s^2, \qquad \varepsilon_2 = 2 n_s \kappa_s \tag{4}$$

where c is the speed of light in vacuum. Here, $\tilde{\varepsilon} = \varepsilon_1 - i\varepsilon_2 = N_s^2$ is the complex relative permittivity of the sample. Thus, $n_s = \mathrm{Re}\{\tilde{\varepsilon}^{1/2}\}$, which differs from $\varepsilon_1^{1/2}$ when κ_s is not small, and ε_1 and ε_2 are the real part and the negative imaginary part of $\tilde{\varepsilon}$. The subscript s is omitted hereafter ($n \equiv n_s$, $\kappa \equiv \kappa_s$).

Errors in ρ propagate into the retrieved index through the derivative of Equation (3),

$$\delta N_s = -\frac{2N_q\, r_{qs}}{(1 + r_{qs})^2}\,\frac{\delta\rho}{\rho} \tag{5}$$

A phase error $\delta\phi$ ($\delta\rho/\rho = i\,\delta\phi$) and a relative amplitude error δa ($\delta\rho/\rho = \delta a$) therefore enter N_s with coefficients that differ by a factor of i. For the quartz–air interface itself ($N_s = 1$), Equation (5) gives $\delta n = -0.82\,\delta a$ and $\delta\kappa = 0.82\,\delta\phi$, so amplitude and phase errors in the transfer of the reference appear separately in the n and α maps of bare quartz. An axial offset Δz between the reference and sample interfaces adds a phase of $4\pi f\Delta z/c$. At 0.5 THz and normal incidence, a 1 μm offset produces an apparent absorption of 3.6 cm^{-1} in a bare quartz–air region.

2.5. Image Analysis and Reflection–Transmission Comparison

Peak-to-peak contrast was calculated as the maximum minus the minimum of each waveform. Spectral-amplitude maps at 0.5 and 1.0 THz were obtained from $|E_s(f)|$, and n, κ, α, ε_1, and ε_2 were calculated from Equations (1)–(4); both frequencies are bins of the discrete Fourier transform of the 48 ps record. Maps of n and α are shown at 0.5 THz, where the spectral amplitude is higher than at 1.0 THz (Figure 2d). Maps of ε_1 and ε_2 are shown at both frequencies to show how the contrast changes with frequency. Because $\tilde{\varepsilon} = N^2$, the permittivity maps at 1.0 THz also determine n and α at that frequency.

Reflection spectra were extracted from 9 × 9-pixel ROIs in the image data, one inside the empty chamber, where the quartz surface is uncovered, as the quartz–air reference and one at the center of each liquid chamber. With a chamber diameter of 9 mm, the ROI edges were about 3 mm from the chamber walls, several times the measured spot width (Section 2.2), so the focused beam stayed within a single material region and did not reach the walls. The quartz–air reference field was first averaged over its ROI at each frequency. The optical constants were then calculated for each sample pixel with this common complex reference and averaged over each sample ROI. Error bars on the reflection data show the spatial standard deviation (SD) over the 81 pixels of the sample ROI at each frequency.

Quantitative comparisons were restricted to 0.5–1.5 THz. Below 0.5 THz, the reflection-derived spectra of all three liquids deviated from the transmission data in the same way. Above 1.5 THz, where the reflected spectral amplitude was less than 10% of that at 0.5 THz (Figure 2d), the spatial SD increased steeply (Section 3.3). In this band ($K = 49$ frequency bins), the agreement between a reflection-derived quantity X_R and the corresponding transmission-derived quantity X_T, interpolated to the same frequencies f_k, was quantified by the root-mean-square (RMS) difference and the RMS relative difference,

$$\mathrm{RMSE} = \left[\frac{1}{K}\sum_{k=1}^{K}\Delta X_k^2\right]^{1/2}, \qquad \mathrm{RMSE}_{\mathrm{rel}} = \left[\frac{1}{K}\sum_{k=1}^{K}\left(\frac{\Delta X_k}{X_T(f_k)}\right)^2\right]^{1/2} \tag{6}$$

where $\Delta X_k = X_R(f_k) - X_T(f_k)$. The mean of ΔX_k over the band is reported as the bias.

2.6. Double-Debye Model

The permittivity spectra were described with a double-Debye model. Debye-type relaxation models are commonly used for water and aqueous mixtures in the THz range [2,10,23]. Because a THz band covers only part of the relaxation spectrum, not all parameters can be fitted: ellipsometry studies of aqueous binary mixtures fixed the dielectric strengths at the literature values and fitted only relaxation times [17,18], and a double Cole–Cole model was used where the relaxations were broadened [15]. In the convention $\tilde{\varepsilon} = \varepsilon_1 - i\varepsilon_2$,

$$\tilde{\varepsilon}(f) = \varepsilon_\infty + \frac{\Delta\varepsilon_{\mathrm{I}}}{1 + i2\pi f\tau_{\mathrm{I}}} + \frac{\Delta\varepsilon_{\mathrm{II}}}{1 + i2\pi f\tau_{\mathrm{II}}} \quad (7)$$

where $\Delta\varepsilon_{\mathrm{I}}$ and τ_{I} describe the slow (cooperative) relaxation of water, $\Delta\varepsilon_{\mathrm{II}}$ and τ_{II} a fast relaxation, and ε_∞ the contributions at higher frequencies. The analysis band lies far above the slow-relaxation frequency, $1/(2\pi\tau_{\mathrm{I}}) \approx 18$ GHz for water. There, the slow term adds approximately $\Delta\varepsilon_{\mathrm{I}}/(2\pi f\tau_{\mathrm{I}})$ to ε_2 and little to ε_1, so the data constrain the ratio $\Delta\varepsilon_{\mathrm{I}}/\tau_{\mathrm{I}}$ but not $\Delta\varepsilon_{\mathrm{I}}$ and τ_{I} separately. We therefore fixed $\tau_{\mathrm{I}} = 8.90$ ps, $\Delta\varepsilon_{\mathrm{II}} = 1.93$, and $\tau_{\mathrm{II}} = 0.224$ ps at the values for water at 22 °C given by the model of Liebe et al. [23] and fitted $\Delta\varepsilon_{\mathrm{I}}$ and ε_∞ to ε_1 and ε_2 of each liquid over 0.5–1.5 THz by least squares. The fitted $\Delta\varepsilon_{\mathrm{I}}$ of a sucrose solution divided by that of water then measures how much the slow-relaxation contribution in this band decreases relative to pure water. With $\Delta\varepsilon_{\mathrm{II}}$ held at its pure-water value, this ratio also absorbs any change in the fast relaxation. Section 3.4 examines the effect of this choice. The Roman subscripts number the relaxations and should not be confused with ε_1 and ε_2.

3. Results

3.1. Concentration-Dependent Optical Properties in Reflection

Figure 2a,b shows the real refractive index and absorption coefficient retrieved from reflection measurements of water and sucrose solutions at 30 and 60 wt%. The retrieval used $N_q = 2.11 - 2.38 \times 10^{-4}\, i$ for quartz (Section 2.1). The refractive indices of the three liquids are relatively close over the displayed range, but the absorption coefficient generally decreases with increasing sucrose concentration. Previous THz measurements of aqueous sugar solutions are consistent with these trends [2]. The data in Figure 2a,b are replotted with error bars in Section 3.3.

Figure 2c shows the ROI-averaged waveforms of the reference and the three liquids. The peak-to-peak amplitude of the interface reflection, relative to that of the reference, was 0.50, 0.36, and 0.22 for water and the 30 and 60 wt% solutions. Well before the interface reflection ($t < 15$ ps), the four waveforms were nearly identical, with amplitudes of up to 6% of the reference peak: each liquid waveform matched the reference waveform with a least-squares scale factor of 1.00–1.02 and a correlation coefficient of at least 0.987. After the pulse ($t > 36$ ps), the scale factors were 1.00–1.01. This part of the signal therefore does not scale with the interface reflection coefficient. The amplitude spectra (Figure 2d) peaked at 0.6 THz for the reference and at 0.25 THz for the liquids, and at 1.5 THz they were 5–9% of their values at 0.5 THz.

The spectra in Figure 2a,b also contain a weak periodic modulation and, below 0.5 THz, larger excursions, such as the peak in n near 0.33 THz. Both are common to the three liquids. After a linear trend was removed, the deviations of the reflection data from the transmission data over 0.5–1.5 THz were strongly correlated between the liquids, with correlation coefficients of 0.83–0.98 for n, α, ε_1, and ε_2. Their RMS amplitude was 0.020–0.025 in n and 8–11 cm^{-1} in α. In a Fourier transform of the detrended deviations (Hann taper, peak searched at delays of 4–15 ps), those in n, ε_1, and ε_2 had a dominant period of about 0.12–0.14 THz. A modulation that is the same for all samples arises from the shared reference or from the measurement system, not from the liquids, whose spectra are expected to be smooth in this range. The inversion itself acts on each frequency separately and cannot create a periodic modulation. The period of the modulation corresponds to signal components 7–8 ps away from the interface reflection, which lie inside the Hann window. Such components cancel in ρ only if they scale with the interface reflection coefficient, and Figure 2c shows that part of the recorded signal does not.

As a check, we narrowed the Hann window applied to the ROI-averaged waveforms from 48 to 16 ps, centered on the interface reflection, so that components 7–8 ps away were strongly attenuated and those farther away were excluded. The periodic modulation then disappeared, the RMS amplitude of the detrended deviations decreased to 0.008–0.010 in n and 5–8 cm^{-1} in α, and the band-averaged n and α changed by less than 0.001 and 1 cm^{-1}, respectively. Narrowing the window is comparable to smoothing the spectra over about 0.1 THz, so the check shows only that the band averages do not depend on the modulation, not where the modulation comes from. The excursions below 0.5 THz became smaller but remained. They are not caused by noise: they far exceed the standard error of the ROI means (below 0.006 in n), and the spectral amplitudes in this range are 0.6–1.5 times those at 0.5 THz (Figure 2d). The spectra and maps were not smoothed or re-windowed, because the full window keeps the frequency resolution of the measurement and the narrower window did not change the band averages. Instead, the quantitative analysis was restricted to 0.5–1.5 THz, and the ranges outside this band are shaded in Figure 2 and in the figures of Section 3.3.

3.2. Transmission Spectra of the Same Solutions

In transmission (Figure 3), the refractive-index curves are smooth and closely spaced, and the absorption increases with frequency. Water has the largest absorption and the 60 wt% sucrose solution the smallest over the displayed interval.

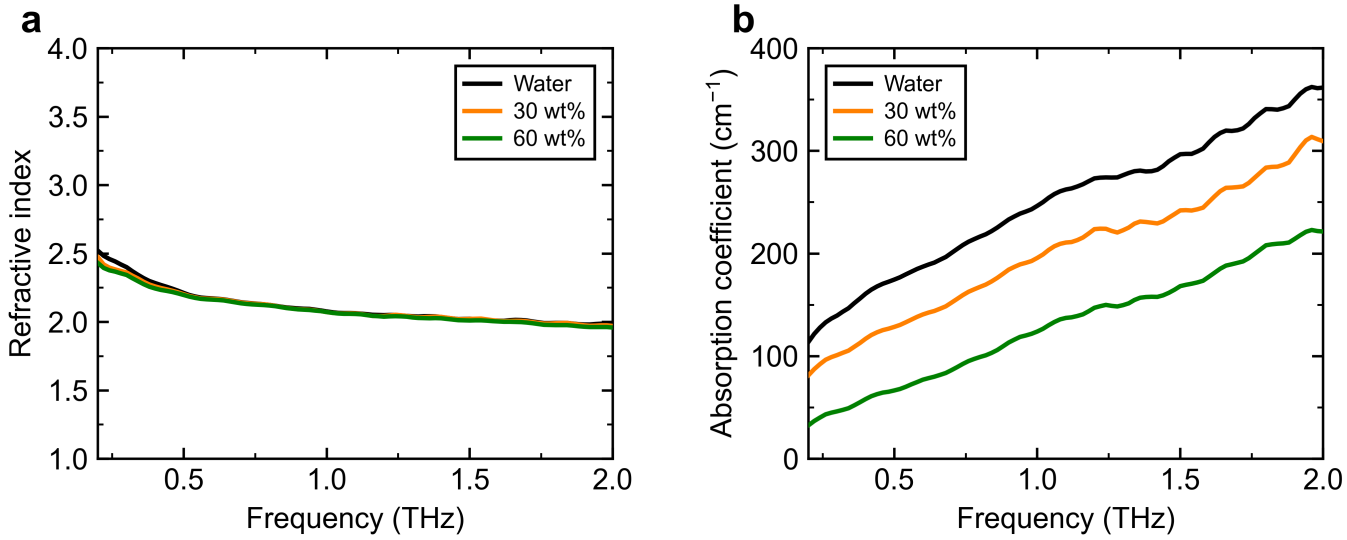


Figure 3. Transmission-derived (**a**) real refractive index and (**b**) power absorption coefficient of water and sucrose solutions at 30 and 60 wt%.

3.3. Direct Comparison of Reflection and Transmission Results

Figures 4–6 compare n, κ, and α obtained in reflection and transmission for water and the two sucrose solutions. The permittivity derived from the same data is shown in Section 3.4. For water (Figure 4), the absorption coefficients from both methods increase with frequency and have a similar spectral shape. The refractive-index spectra from the two methods also show a similar frequency dependence. The comparisons for 30 wt% sucrose solution (Figure 5) and 60 wt% sucrose solution (Figure 6) show that the reflection and transmission spectra again agree in shape. With both methods, the absorption is generally lower at higher sucrose concentrations (Figures 2 and 3).

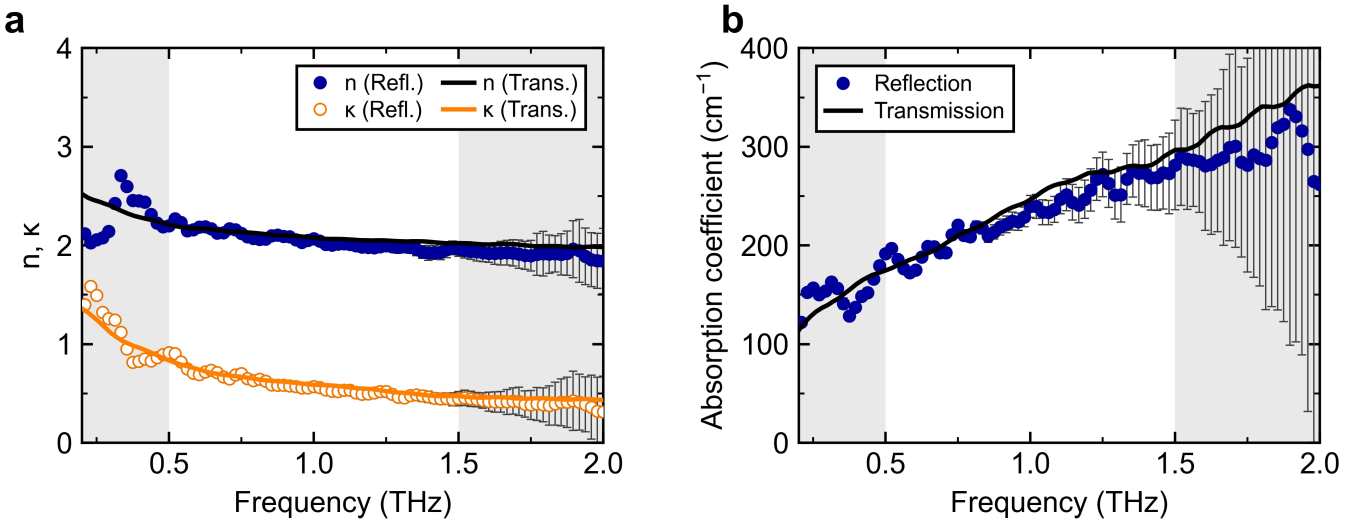


Figure 4. Comparison of reflection- and transmission-derived properties for water: (**a**) real refractive index and extinction coefficient and (**b**) power absorption coefficient. Reflection markers show the means of 81 pixels within a 9 × 9-pixel ROI, and error bars show their spatial standard deviations; error bars smaller than the markers are hidden by them. Transmission spectra are shown as lines. Shaded areas lie outside the 0.5–1.5 THz band used for quantitative comparison.

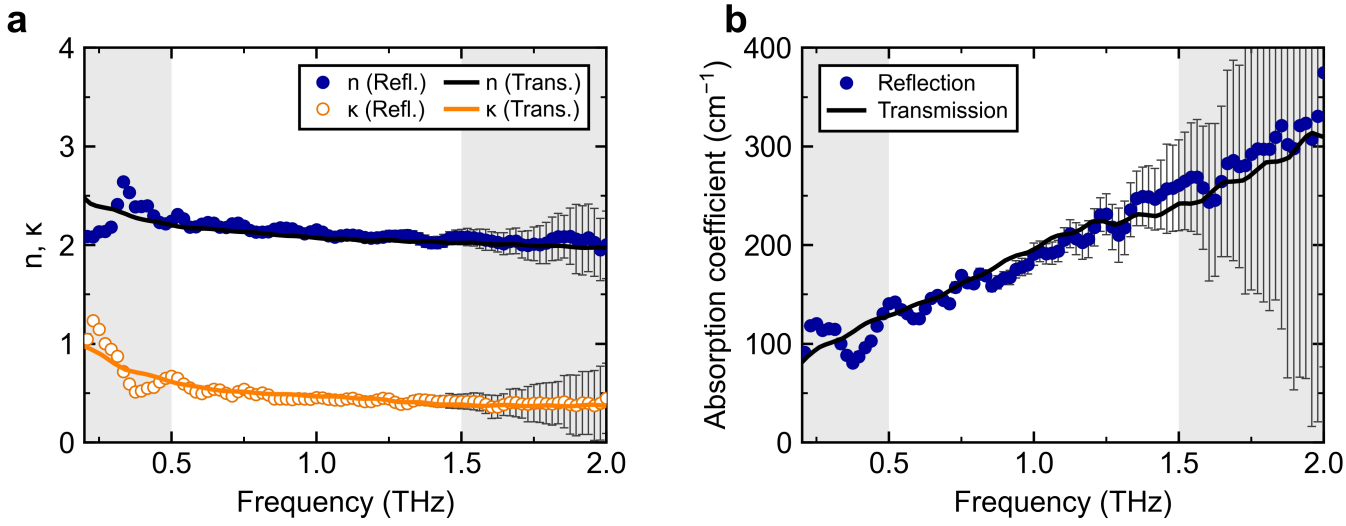


Figure 5. (**a**,**b**) Comparison of reflection- and transmission-derived properties for the 30 wt% sucrose solution (panels as in Figure 4). Reflection markers and error bars show the 81-pixel ROI means and spatial standard deviations, respectively (error bars smaller than the markers are hidden). Transmission spectra are shown as lines, and shaded areas lie outside the 0.5–1.5 THz band.

Table 1 lists the values at the two map frequencies, and Table 2 gives the differences between the two methods over 0.5–1.5 THz. In this band, the RMS relative difference was 2.4–3.4% for n, 5.9–8.9% for α, 5.0–6.9% for ε_1, and 6.3–9.2% for ε_2. The bias of n was −0.038, +0.044, and −0.069 for water and the 30 and 60 wt% solutions, and the bias of α was within 10 cm^{-1}. At 1.0 THz, the reflection-derived α of the three liquids was within 3% of the transmission values and ε_2 within 4%. At 0.5 THz, the reflection-derived α exceeded the transmission values by 10%, 9%, and 31%. This frequency lies near a maximum of the common modulation (Section 3.1, Figure 2b).

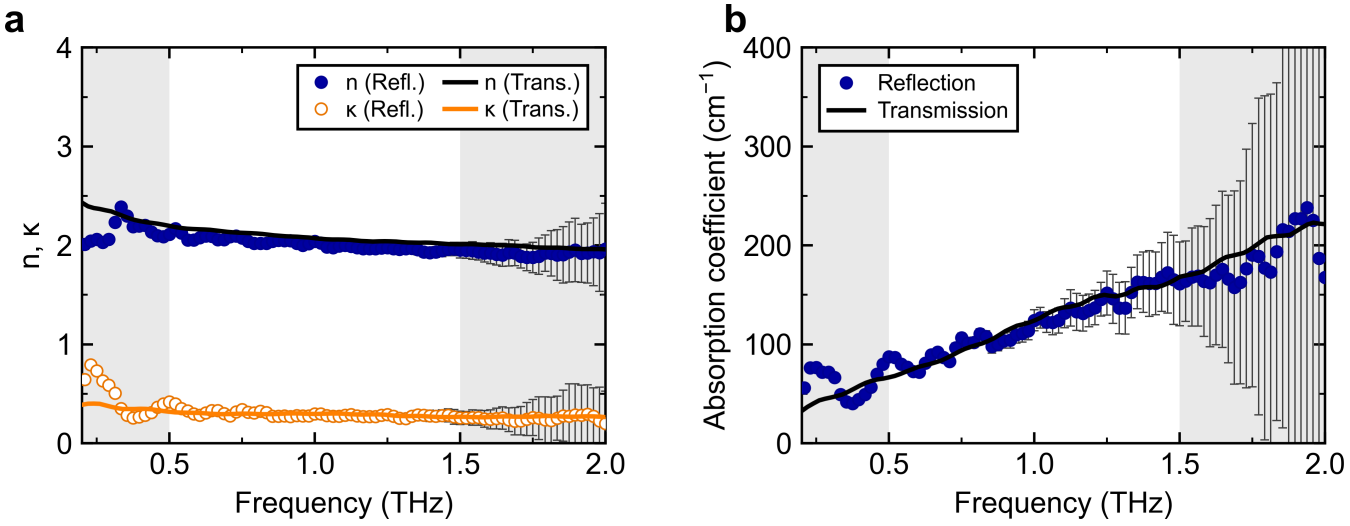


Figure 6. (**a**,**b**) Comparison of reflection- and transmission-derived properties for the 60 wt% sucrose solution (panels as in Figure 4). Reflection markers and error bars show the 81-pixel ROI means and spatial standard deviations, respectively (error bars smaller than the markers are hidden). Transmission spectra are shown as lines, and shaded areas lie outside the 0.5–1.5 THz band.

Table 1. Optical constants at the map frequencies, 0.5 and 1.0 THz. Reflection values are ROI means ± spatial SD over 81 pixels; transmission values are interpolated to the same frequencies. α is in cm^{-1}.

Liquid	Method	0.5 THz				1.0 THz			
		n	α	ε_1	ε_2	n	α	ε_1	ε_2
Water	Refl.	2.20 ± 0.03	192 ± 4	4.00 ± 0.14	4.02 ± 0.12	2.07 ± 0.04	240 ± 11	3.95 ± 0.17	2.37 ± 0.14
	Trans.	2.21	175	4.20	3.69	2.08	246	3.97	2.44
30 wt%	Refl.	2.24 ± 0.03	141 ± 4	4.58 ± 0.12	3.01 ± 0.09	2.15 ± 0.04	191 ± 11	4.44 ± 0.18	1.96 ± 0.12
	Trans.	2.20	129	4.48	2.70	2.07	196	4.07	1.94
60 wt%	Refl.	2.11 ± 0.02	87 ± 4	4.29 ± 0.09	1.76 ± 0.08	2.04 ± 0.03	124 ± 11	4.08 ± 0.10	1.21 ± 0.11
	Trans.	2.20	67	4.73	1.40	2.07	124	4.21	1.23

Table 2. Differences between reflection- and transmission-derived values over 0.5–1.5 THz (49 frequency bins): RMS difference (RMSE), RMS relative difference (RMSE$_{rel}$, %), and bias (mean of reflection minus transmission), Equation (6).

Quantity	Water			30 wt% Sucrose			60 wt% Sucrose		
	RMSE	Rel. (%)	Bias	RMSE	Rel. (%)	Bias	RMSE	Rel. (%)	Bias
n	0.054	2.6	−0.038	0.051	2.4	+0.044	0.072	3.4	−0.069
α (cm^{-1})	14.6	5.9	−9.9	12.2	6.3	−1.9	8.5	8.9	−0.7
ε_1	0.20	5.0	−0.13	0.23	5.4	+0.19	0.30	6.9	−0.28
ε_2	0.20	7.9	−0.12	0.13	6.3	+0.01	0.12	9.2	−0.03

As a check against established data, the water spectra were compared with the literature values for water at 20–25 °C. At 1.0 THz, these values range from 2.08 to 2.13 for n and from 224 to 241 cm^{-1} for α [2,23,24]. Our values of n (2.07 from reflection, 2.08 from transmission) are close to the lower end of the range for n, and our values of α (240 and 246 cm^{-1}) are at or slightly above the upper end of the range for α. Over 0.5–1.0 THz, where the double-Debye model of Liebe et al. is valid [23], the reflection-derived n and α of water deviated from this model for 22 °C by −2.8% and +5.5% on average, and the transmission-derived values by

−2.2% and +7.2%. The two methods thus deviate from the model in the same direction and by similar amounts, so these deviations are not specific to the in-plane reference.

3.4. Complex Permittivity and Double-Debye Analysis

Figure 7 shows ε_1 and ε_2 of the three liquids from reflection over 0.5–1.5 THz, together with double-Debye fits (Equation (7)). The loss term ε_2 decreased with increasing sucrose concentration over the whole band, from 2.37 for water to 1.96 and 1.21 for the 30 and 60 wt% solutions at 1.0 THz (Table 1). The real part ε_1 of all three liquids decreased with frequency, from 4.0–4.6 at 0.5 THz to 3.7–4.2 at 1.5 THz, and the differences between the liquids were comparable to the differences between the reflection and transmission results (Table 2).

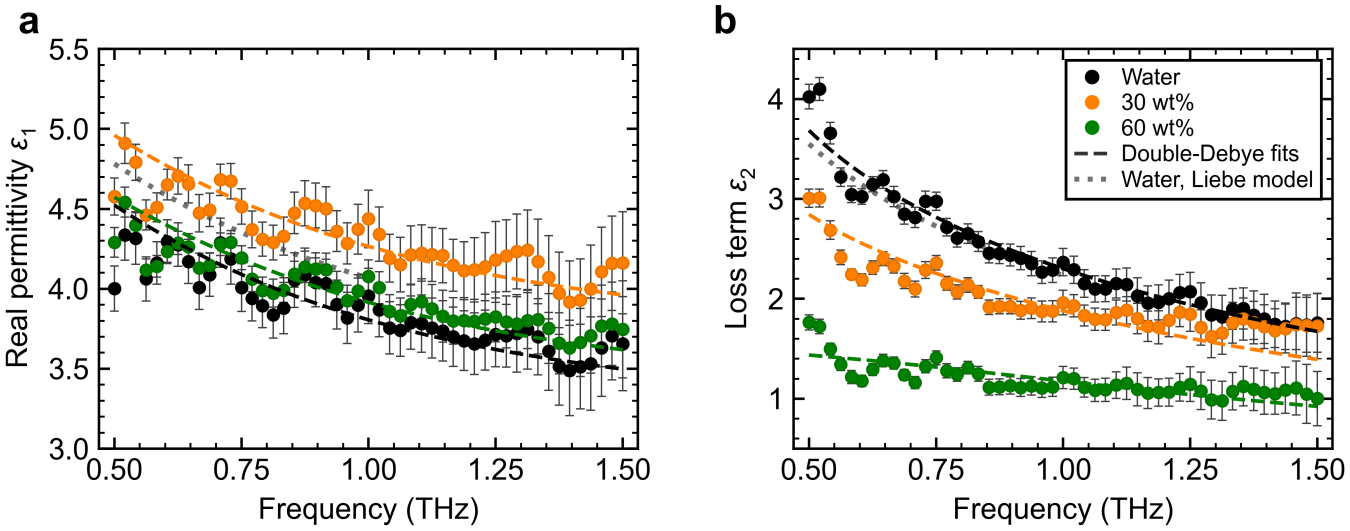


Figure 7. Reflection-derived (**a**) real permittivity ε_1 and (**b**) loss term ε_2 of water and sucrose solutions at 30 and 60 wt% over 0.5–1.5 THz. Markers show the ROI means, and error bars show the spatial standard deviations. Dashed lines, in the color of each liquid, are double-Debye fits (Equation (7)) with τ_I, $\Delta\varepsilon_{II}$, and τ_{II} fixed at the values for water at 22 °C; the dotted gray line is the model of Liebe et al. for water at 22 °C [23], shown up to 1.0 THz, the upper limit of the model. The legend in (**b**) applies to both panels.

With τ_I, $\Delta\varepsilon_{II}$, and τ_{II} fixed at the values for water, the two-parameter model reproduced ε_1 and ε_2 with RMS residuals of 0.08–0.16 (Table 3). For the reflection data, these residuals are comparable to the common modulation, so a broadening parameter, as in a double Cole–Cole model [15], would not be constrained by these data. For water, the fitted $\Delta\varepsilon_I$ was 77.8 from reflection and 81.5 from transmission, 5% and 10% larger than the value of 74.0 in the model of Liebe et al. [23], in line with the higher absorption of our water data. Relative to water, $\Delta\varepsilon_I$ decreased to 0.70 (reflection) and 0.66 (transmission) for the 30 wt% solution and to 0.19 for the 60 wt% solution with both methods, so reflection and transmission gave the same concentration dependence within 0.05. If sucrose only diluted the water, these ratios would equal the volume fraction of water, 0.79 and 0.52 for the two solutions, calculated from their densities of 1.127 and 1.287 g/cm^3 [25]. With the fast relaxation held at its pure-water strength, the smaller ratios indicate that the slow-relaxation contribution in the THz band decreases faster than the water content. If $\Delta\varepsilon_{II}$ is instead scaled by ϕ_w, the ratios become 0.81 (reflection) and 0.77 (transmission) for the 30 wt% solution, near its water volume fraction, and 0.45 and 0.43 for the 60 wt% solution, still below 0.52. Only the result for the 60 wt% solution is independent of this choice. With τ_I and τ_{II} taken from the water data of Rønne et al. [10], interpolated to 22 °C (8.1 and 0.18 ps; $\Delta\varepsilon_{II}$ = 1.93 in both sets), all of these

ratios changed by less than 0.01. With only $\Delta\varepsilon_I/\tau_I$ constrained, the faster decrease at 60 wt% may come from a smaller relaxation strength, a longer relaxation time, or both, as expected if water in the hydration shells of sugars relaxes more slowly than bulk water. Such slower dynamics were found for sucrose and trehalose solutions [26] and in simulations of lactose solutions [27]. In acetone–water mixtures, the slow-relaxation strength decreased strongly while the fast-relaxation strength stayed nearly constant [15], and the deviations of 2-propanol–water mixtures from an ideal-mixture Debye model were described by a change in the slow relaxation time [17]. Our data cannot distinguish between these two descriptions.

Table 3. Double-Debye parameters fitted over 0.5–1.5 THz with τ_I = 8.90 ps, $\Delta\varepsilon_{II}$ = 1.93, and τ_{II} = 0.224 ps fixed. Uncertainties are standard errors of the fit and do not include systematic errors. ϕ_w is the volume fraction of water, and the last column gives the RMS fit residuals for reflection/transmission.

Liquid	$\Delta\varepsilon_I$		ε_∞		$\Delta\varepsilon_I/\Delta\varepsilon_{I,water}$		ϕ_w	RMS Residual
	Refl.	Trans.	Refl.	Trans.	Refl.	Trans.		
Water	77.8 ± 0.9	81.5 ± 1.1	3.13 ± 0.02	3.26 ± 0.02	1	1	1	0.13/0.16
30 wt%	54.2 ± 1.1	53.7 ± 0.8	3.60 ± 0.02	3.40 ± 0.02	0.70 ± 0.02	0.66 ± 0.01	0.79	0.16/0.12
60 wt%	14.8 ± 0.8	15.3 ± 0.5	3.26 ± 0.02	3.54 ± 0.01	0.19 ± 0.01	0.19 ± 0.01	0.52	0.11/0.08

3.5. Reflection-Contrast and Spectral-Amplitude Maps

Reflection images were acquired from a four-region target containing a sample-free quartz–air reference, water, 30 wt% sucrose solution, and 60 wt% sucrose solution. Figure 8 shows a time-domain peak-to-peak reflection map and spectral-amplitude maps at 0.5 and 1.0 THz. All three liquids are colorless, but they differ in the THz maps. The reflected signal is highest in the empty chamber and decreases in the order water, 30 wt% sucrose solution, and 60 wt% sucrose solution. The maps also separate the circular sample regions from the chamber structure and the surrounding uncovered quartz. Between the chambers, the beam is reflected at the interface between the quartz and the adhesive silicone gasket of the chamber structure, not at bare quartz, so the values retrieved there are effective values of this contact rather than bulk properties of silicone.

The measured amplitude contrast arises from the complex Fresnel reflection coefficients at the quartz–air and quartz–sample interfaces. The large index mismatch between quartz and air produces a strong reference reflection. Because the reflection coefficient depends on both the real and imaginary parts of the sample index, the brightness of an amplitude image alone does not specify an intrinsic refractive index or absorption coefficient. We therefore divided the complex field (amplitude and phase) at each pixel by the field averaged over the quartz–air reference ROI in the empty chamber and obtained maps of the optical constants from Equations (1)–(4).

3.6. Maps of Refractive Index, Absorption, and Permittivity

Figure 9 shows maps of the real refractive index and power absorption coefficient retrieved at 0.5 THz using the in-plane quartz–air reference. As expected, the empty chamber, which contains the reference ROI, has n close to 1 and α close to 0 cm^{-1}. Water and the two sucrose solutions have similar refractive indices, although the value for the 60 wt% sucrose solution is slightly lower, by about its reflection–transmission bias (Table 2). The absorption map separates the three liquid regions more clearly. The mapped α is highest for water and lowest for the 60 wt% sucrose solution, as in the reflection spectra of Figure 2.

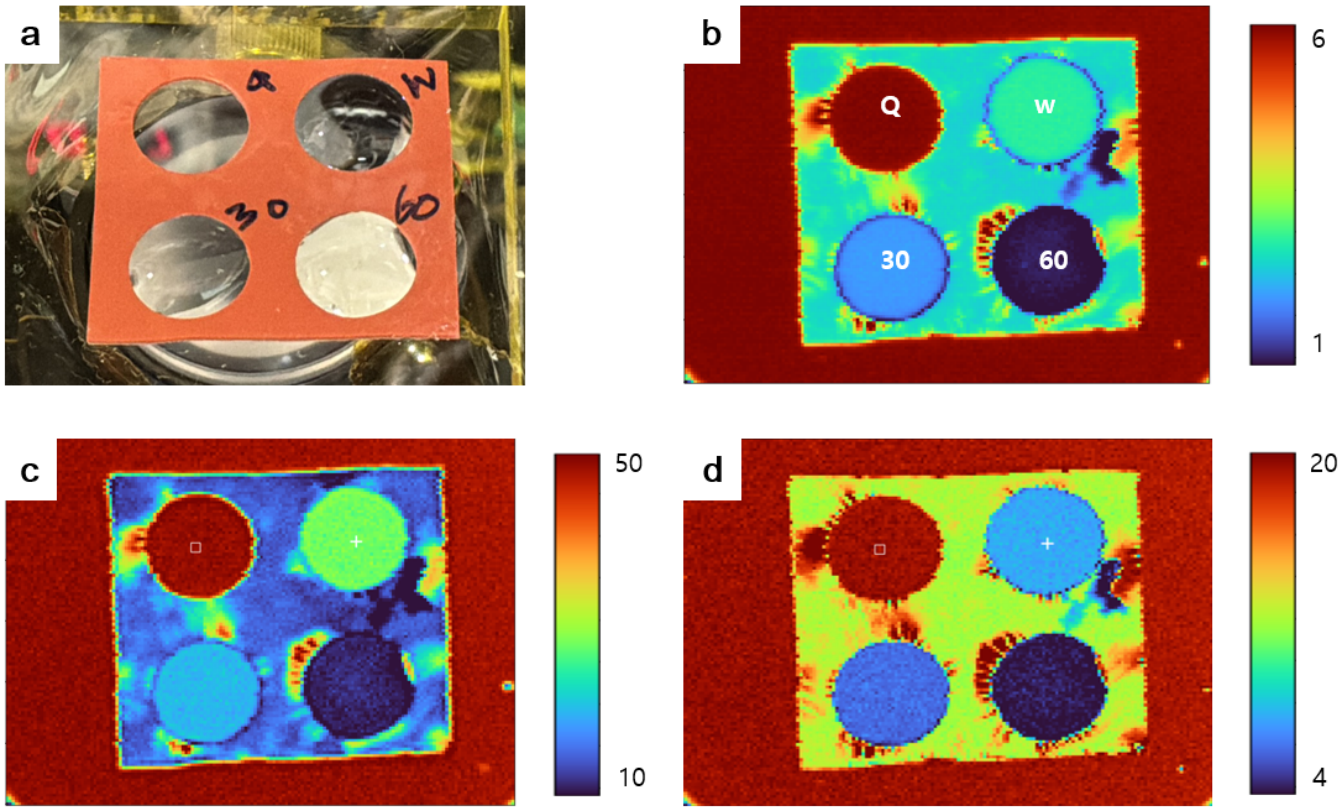


Figure 8. Four-region target: (**a**) photograph and reflection images of (**b**) time-domain peak-to-peak amplitude, (**c**) spectral amplitude at 0.5 THz, and (**d**) spectral amplitude at 1.0 THz. Q, w, 30, and 60 denote the quartz–air reference region, water, 30 wt% sucrose solution, and 60 wt% sucrose solution, respectively.

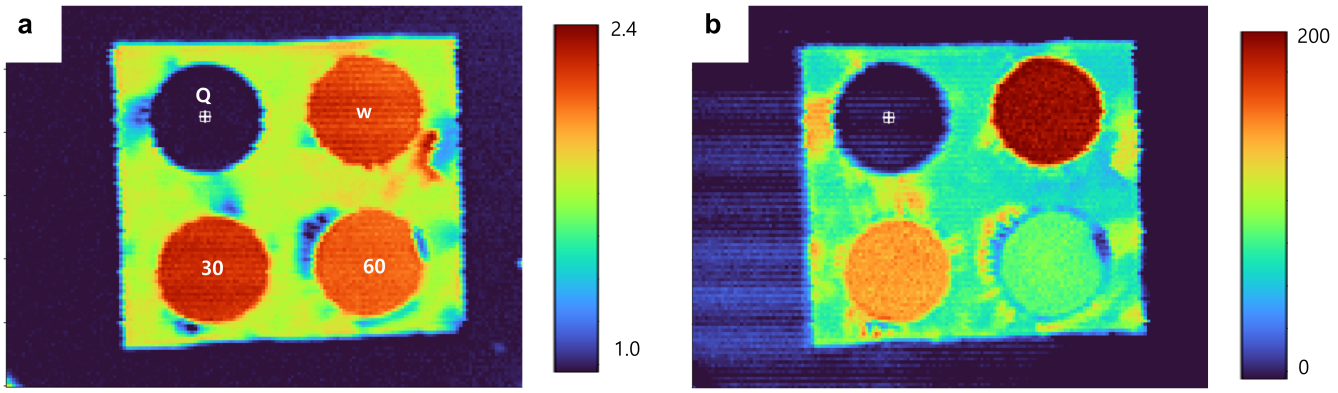


Figure 9. Quantitative reflection images at 0.5 THz of (**a**) real refractive index and (**b**) power absorption coefficient retrieved with the in-plane quartz–air reference. Q, w, 30, and 60 denote the quartz–air reference region, water, 30 wt% sucrose solution, and 60 wt% sucrose solution, respectively.

Unlike the peak-to-peak and spectral-amplitude maps in Figure 8, the maps in Figure 9 give n and α separately for each region. The 60 wt% sucrose solution, for example, produces the weakest reflection in Figure 8, but Figure 9 shows that its refractive index is close to those of the other two liquids and that its absorption is the lowest. Outside the chamber structure, where the quartz surface is bare, n and α are close to their values in the empty chamber. Most of the chamber structure has a lower refractive index than the 60 wt% sucrose solution but a similar absorption coefficient in these maps. The chamber structure is not uniform: over most of it, n was 1.71–1.78 and α was 67–85 cm^{-1} (interquartile ranges), with larger deviations near its cut edges and next to the chambers. Regions with n close to 1,

such as the crescent-shaped areas next to the water and 60 wt% chambers, behave like a quartz–air interface and indicate air gaps or trapped air where the gasket did not adhere fully to the quartz.

To test the choice of ROI size, the mean n and α at 0.5 THz were recalculated from the maps for square ROIs of up to 21 × 21 pixels (5.25 × 5.25 mm^2) centered in each chamber. Compared with the 9 × 9-pixel ROIs, the mean n changed by less than 1% and the mean α by less than 3%, and the spatial SD of α changed by less than 20%. For 25 × 25 pixels, the ROI corners approached the chamber walls and the SD of α increased by a factor of 1.5–3. The results are therefore insensitive to the ROI size as long as the ROI stays away from the walls.

The bare quartz–air area surrounding the chamber structure has known optical constants, and its retrieved values test how well the reference measured in the empty chamber applies elsewhere in the image. In this area, ε_1 at 1.0 THz was 0.99–1.01 with an SD of at most 0.03 at distances of up to about 30 mm from the reference ROI, so amplitude errors in the reference transfer are below about 2% (Equation (5)). Phase errors appear instead as an apparent absorption (3.6 cm^{-1} per micrometer of axial offset at 0.5 THz; Section 2.4). To the left of the chamber structure, α was 6 ± 6 cm^{-1} with stripes along the scan lines, corresponding to a phase error of about 0.04 rad or an axial offset of about 2 µm. In the other bare-quartz areas, the apparent α was mostly at or below the lower limit of the color scale in Figure 9b (0 cm^{-1}), so the phase error there was smaller or of opposite sign, and its size is not resolved by the figure. The bare quartz thus shows a small phase gradient across the field, as expected for a slight tilt of the window relative to the scan plane, and fitting a plane to the apparent phase of the bare quartz would remove it. At the wall of the empty chamber, the 10–90% width of the transition was about 0.5 mm in the n map at 0.5 THz and about 0.4 mm in the ε_1 map at 1.0 THz. These widths are comparable to the 10–90% width of the knife-edge response (0.45–0.54 mm, depending on the fit; Section 2.2). At 1.0 THz, the width is close to the resolution set by the 0.25 mm scan step.

Maps of ε_1 and the positive loss term ε_2 at 0.5 and 1.0 THz (Figure 10) were calculated from the complex refractive index at each pixel with Equation (4). The ε_1 maps largely follow the n map in Figure 9a, except that water, which has the largest κ, has the lowest ε_1 of the three liquids. The ε_2 maps largely follow the distribution of κ, which at 0.5 THz is proportional to α (Figure 9b).

Weak stripes along the scan lines are visible inside the liquid chambers in the n and ε_1 maps (Figures 9a and 10a,c). In each liquid chamber, the line-averaged n alternated between adjacent scan lines. The mean difference between even and odd lines was 0.018–0.040 in n at 0.5 THz (Welch's t-test on the line means, $p \leq 0.001$ in all three liquids), which corresponds by Equation (5) to a phase difference of 0.040–0.044 rad. At 1.0 THz, the phase difference obtained in the same way from the ε_1 maps was 0.08–0.09 rad. A phase difference that grows in proportion to frequency is a time shift, here 12–14 fs, or an axial offset of about 2 µm, between adjacent scan lines. For the liquids, such an error changes mainly n and ε_1, whereas for bare quartz it changes α and ε_2 (Section 2.4). This is why the stripes appear in the liquid regions of the n and ε_1 maps and in the bare-quartz regions of the α and ε_2 maps (Figures 9b and 10d).

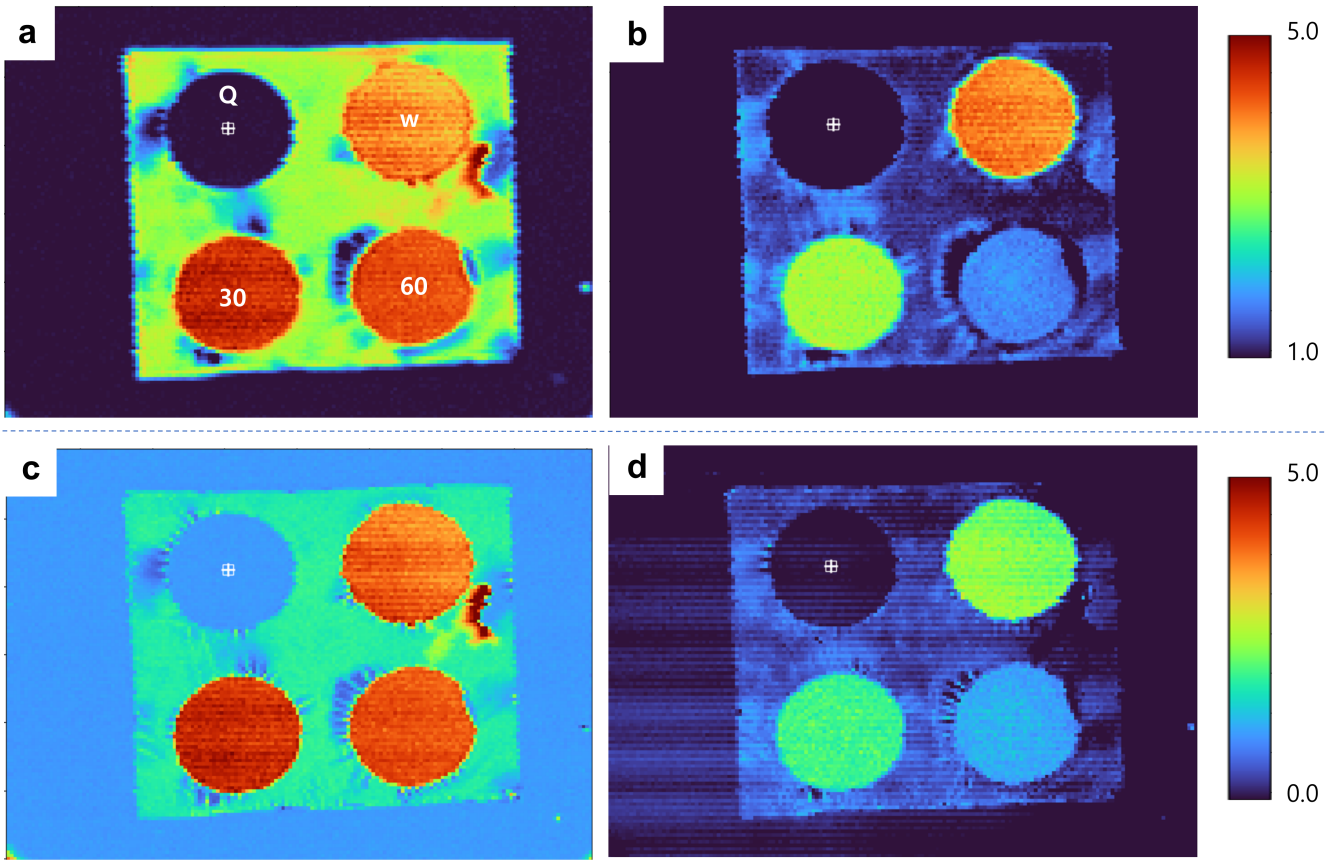


Figure 10. Complex-permittivity images showing (**a**) the real permittivity ε_1 and (**b**) the positive loss term ε_2 at 0.5 THz, and (**c**) ε_1 and (**d**) ε_2 at 1.0 THz. Each color scale applies to both panels in its row. The sign convention is $\tilde{\varepsilon} = \varepsilon_1 - i\varepsilon_2$. Q, w, 30, and 60 denote the quartz–air reference region, water, 30 wt% sucrose solution, and 60 wt% sucrose solution, respectively.

4. Discussion

The in-plane quartz–air reference lies on the same quartz surface as the samples and is recorded in the same scan. The time-independent part of the system response is therefore nominally common to both and cancels in their complex-field ratio. The known quartz–air Fresnel coefficient can then be used as a local complex-field standard, and the samples need not be replaced by a metal reflector. The raster scan, however, records the reference and sample pixels at different times, and drift of the system during the scan does not cancel. The transfer errors measured in the bare quartz–air area, which every scan line crosses (Section 3.6), include this drift.

Equations (1)–(3) assume normal incidence, but a focused beam also contains oblique rays. For an incident cone with the nominal NA of 0.64 in air, Snell's law with the real quartz index $n_q = 2.11$ limits the ray angles inside quartz to 17.7°. To estimate the resulting error, we averaged the s- and p-polarized Fresnel coefficients of the quartz–air and quartz–liquid interfaces over the angular spectrum of the focused beam, assuming either uniform or Gaussian filling of the aperture up to this NA, and inverted the resulting ratio with Equation (3). For the three liquids between 0.5 and 1.5 THz, the retrieved n changed by less than 0.04% and κ by up to about 0.3%. The error is small because the angles in quartz are moderate, the s- and p-polarized coefficients deviate from their normal-incidence values in opposite directions, and the reference and sample interfaces have similar angular dependences. The normal-incidence inversion is therefore adequate for this geometry, and the finite NA cannot explain the reflection–transmission differences in Table 2.

Errors in the phase of the reference matter more. By Equation (5), a phase error of 0.01 rad changes n of water by 0.010 at 0.5 THz and by 0.006 at 1.0 THz. Misplacing a separately measured reference reflector is a known source of such errors [5–7]. A reflector displaced axially by Δz from the sample interface adds a phase of $4\pi f \Delta z/c$. For a displacement of 10 µm, inversion with Equation (3) changes the retrieved n of water by 0.19–0.25 (9–12%) at 0.5–1.0 THz and α by up to 37 cm^{-1} (15%) at 1.0 THz. In the in-plane geometry, the reference and samples share one quartz surface. In the bare quartz to the left of the target, the residual axial offset was about 2 µm, which would change n of the liquids by 0.02–0.05. On the other sides, the offset was smaller or of opposite sign (Section 3.6). The line-to-line alternation of similar size averages out in the ROI means. The amplitude transfer was accurate to about 2%, which changes κ by about 2%. These residual errors and the common modulation (RMS 0.020–0.025 in n) are of the same size as the reflection–transmission differences in n (RMS 0.05–0.07, Table 2). The transmission values are not exact either. A 3% error in the nominal 184 µm spacer thickness would change the transmission-derived α by 3% and n by 0.03–0.04. The transmission-derived n comes from the phase delay across this thin layer, and a constant phase error of 0.1 rad in the transmission ratio would change it by 0.05 at 0.5 THz and 0.03 at 1.0 THz.

The line-to-line time shift behind the stripes in Figures 9 and 10 (Section 3.6) points to the scanning hardware. The image was recorded with a bidirectional raster scan (Section 2.2), in which a small difference in stage height or tilt between the two scan directions produces such an alternation. Each ROI covers nine scan lines and averages over both line sets. The alternation therefore appears as stripes around the mean values and biases the ROI means by less than 0.002 in n. Because each scan line crosses the bare quartz–air area at its ends, line-wise referencing to these pixels would remove offsets that are constant along a line, and unidirectional scanning or a stage with smaller height and tilt errors would reduce them at the source. Line-wise referencing requires a reference region in every scan line, which the in-plane geometry provides.

Sucrose was chosen with dielectric phantoms for magnetic resonance imaging (MRI) in mind. In reported MRI phantom formulations, NaCl is used primarily to tune radiofrequency conductivity, whereas sucrose is used to lower the permittivity of water-rich mixtures [28,29]. Formulations containing water, NaCl, and sucrose have also been used to construct phantoms representing several tissue types, including cancer-mimicking compartments [30]. The permittivity of such mixtures depends on composition and frequency, so the THz permittivity measured here differs from that at MRI radiofrequencies. The present THz spectra and maps could be combined with radiofrequency data for the same solutions to design phantoms whose dielectric properties are known at both THz and MRI frequencies.

In both the reflection and transmission spectra, the absorption coefficient generally decreases from water to 30 wt% sucrose solution and then to 60 wt% sucrose solution. The spatial spread of the reflection-derived values in Figures 4–6, however, increases with frequency, for α from about 4 cm^{-1} at 0.5 THz to 11 cm^{-1} at 1.0 THz and 42–46 cm^{-1} at 1.5 THz, and becomes large above approximately 1.5 THz. One possible reason is that the complex Fresnel inversion is sensitive to phase uncertainty (Equation (5)), which grows as the reflected spectral amplitude decreases at higher frequencies (Figure 2d). Better phase stability and reference-field calibration should reduce this spread. A direct comparison with a metal reference in the same setup was not part of this study. The error estimates above and the comparisons with the transmission and literature data were used instead.

In Figure 9, the refractive-index map distinguishes regions with similar mapped absorption, such as the chamber structure and the 60 wt% sucrose solution. In biomedical reflection imaging, the same contrast may help to distinguish tissue components that absorb

similarly but differ in refractive index. Adjacent in-plane air referencing could also be applied to small or microfluidic samples that require tightly focused THz beams. Other substrates may replace quartz in this reference geometry if their complex optical constants are known, their transmission is adequate in the measurement band, and the substrate–sample reflection can be isolated in time. For thin films or two-dimensional materials, the measured complex-field ratio can be analyzed with a multilayer or sheet-conductivity model in place of the bulk-interface inversion used here.

5. Conclusions

Instead of a separately measured metal reflector, an adjacent quartz–air region recorded in the same scan and at the same nominal focal plane as the samples provided the complex-field reference for quantitative reflection THz imaging. Complex Fresnel inversion including quartz absorption converted the sample-to-reference field ratio into maps of n, α, ε_1, and ε_2. For water and sucrose solutions at 30 and 60 wt%, the reflection-derived n, α, and permittivity agreed with transmission measurements over 0.5–1.5 THz within RMS relative differences of 3.4%, 8.9%, and 9.2%, respectively. At 1.0 THz, ε_1 was 3.95, 4.44, and 4.08 and ε_2 was 2.37, 1.96, and 1.21 for water and the 30 and 60 wt% solutions. In a double-Debye fit with the fast relaxation of water held fixed, the slow-relaxation contribution decreased to 0.70 and 0.19 of its value for water. For the 60 wt% solution, the decrease exceeded dilution even when the fast term was scaled with the water content. The estimated error from oblique rays in the focused beam was about 0.3% or less. In the bare quartz–air area of the same image, the amplitude error of the reference transfer was below about 2%, and the apparent absorption revealed a residual phase gradient across the field, with an axial offset of about 2 μm on one side of the target. The index and absorption maps distinguished the liquid chambers from the surrounding chamber structure and uncovered quartz–air regions and, unlike the amplitude images, gave the refractive and absorptive responses separately. The optical constants measured for the sucrose solutions may be useful in designing dielectric phantoms intended for both THz imaging and MRI.

Author Contributions: Conceptualization, Y.B.J., S.J.O. and H.-C.R.; methodology, S.J.O.; formal analysis, H.-C.R.; investigation, L.-H.Y. and I.M.; data curation, H.S.B., H.J.S., E.S.L. and H.-C.R.; writing—original draft preparation, L.-H.Y., I.M., S.J.O. and H.-C.R.; writing—review and editing, S.J.O. and H.-C.R.; visualization, H.S.B.; supervision, H.-C.R.; project administration, H.-C.R.; funding acquisition, H.-C.R. All authors have read and agreed to the published version of the manuscript.

Funding: This research was funded by the Sahmyook University Research Fund in 2024.

Institutional Review Board Statement: Not applicable.

Informed Consent Statement: Not applicable.

Data Availability Statement: The data presented in this study are available on request from the corresponding authors.

Conflicts of Interest: The authors declare no conflicts of interest. The funders had no role in the design of the study; in the collection, analyses, or interpretation of data; in the writing of the manuscript; or in the decision to publish the results.

References

1. Son, J.-H. (Ed.) *Terahertz Biomedical Science and Technology*, 1st ed.; CRC Press: Boca Raton, FL, USA, 2014.
2. Jepsen, P.U.; Møller, U.; Merbold, H. Investigation of aqueous alcohol and sugar solutions with reflection terahertz time-domain spectroscopy. *Opt. Express* **2007**, *15*, 14717–14737. [CrossRef]

3. Lin, H.; Braeuninger-Weimer, P.; Kamboj, V.S.; Jessop, D.S.; Degl'Innocenti, R.; Beere, H.E.; Ritchie, D.A.; Zeitler, J.A.; Hofmann, S. Contactless graphene conductivity mapping on a wide range of substrates with terahertz time-domain reflection spectroscopy. *Sci. Rep.* **2017**, *7*, 10625. [CrossRef]
4. Maeng, I.; Lee, Y.M.; Park, J.; Oh, S.J.; Jung, M.-C. Terahertz time-domain spectroscopy as a defect fingerprinting tool for halide perovskite solar cells: Toward a universal framework. *Nanomaterials* **2026**, *16*, 1072. [CrossRef]
5. Lucarini, V.; Ino, Y.; Peiponen, K.-E.; Kuwata-Gonokami, M. Detection and correction of the misplacement error in terahertz spectroscopy by application of singly subtractive Kramers–Kronig relations. *Phys. Rev. B* **2005**, *72*, 125107. [CrossRef]
6. Koalla, R.; Chaudhary, A.K. Cross-correlation technique for phase error correction in reflection mode terahertz time-domain spectroscopy. *Appl. Opt.* **2024**, *63*, 4762–4772. [CrossRef]
7. Han, J.W. Error analysis of complex refractive index obtained from reflection-type THz time-domain spectroscopy with phase mismatching condition. *J. Laser Appl.* **2025**, *37*, 012039. [CrossRef]
8. Ji, Y.B.; Lee, E.S.; Kim, S.-H.; Son, J.-H.; Jeon, T.-I. A miniaturized fiber-coupled terahertz endoscope system. *Opt. Express* **2009**, *17*, 17082–17087. [CrossRef]
9. Fan, S.; Parrott, E.P.J.; Ung, B.S.-Y.; Pickwell-MacPherson, E. Calibration method to improve the accuracy of THz imaging and spectroscopy in reflection geometry. *Photonics Res.* **2016**, *4*, A29–A35. [CrossRef]
10. Rønne, C.; Thrane, L.; Åstrand, P.-O.; Wallqvist, A.; Mikkelsen, K.V.; Keiding, S.R. Investigation of the temperature dependence of dielectric relaxation in liquid water by THz reflection spectroscopy and molecular dynamics simulation. *J. Chem. Phys.* **1997**, *107*, 5319–5331. [CrossRef]
11. Young, J.J.; Agarwal, A.; Page, B.G.; Dogra, A.; Hernandez-Serrano, A.I.; Hardwicke, J.; Pickwell-MacPherson, E. Robotically controlled terahertz probe for in vivo skin evaluation: Imaging with the PicoBot. *J. Infrared Millim. Terahertz Waves* **2025**, *46*, 36. [CrossRef]
12. Huang, S.; Ashworth, P.C.; Kan, K.W.C.; Chen, Y.; Wallace, V.P.; Zhang, Y.-T.; Pickwell-MacPherson, E. Improved sample characterization in terahertz reflection imaging and spectroscopy. *Opt. Express* **2009**, *17*, 3848–3854. [CrossRef]
13. Chen, X.; Parrott, E.P.J.; Ung, B.S.-Y.; Pickwell-MacPherson, E. A robust baseline and reference modification and acquisition algorithm for accurate THz imaging. *IEEE Trans. Terahertz Sci. Technol.* **2017**, *7*, 493–501. [CrossRef]
14. Chernomyrdin, N.V.; Skorobogatiy, M.; Gavdush, A.A.; Musina, G.R.; Katyba, G.M.; Komandin, G.A.; Khorokhorov, A.M.; Spektor, I.E.; Tuchin, V.V.; Zaytsev, K.I. Quantitative super-resolution solid immersion microscopy via refractive index profile reconstruction. *Optica* **2021**, *8*, 1471–1480. [CrossRef]
15. Mazaheri, Z.; Ramankandath, A.; Yaseen, J.; Koral, C.; Papari, G.P.; Andreone, A. THz ATR-TDS spectroscopy of acetone–water mixtures: Hydrogen bonding to dipole–dipole dynamics. *Int. J. Mol. Sci.* **2026**, *27*, 5188. [CrossRef]
16. Lordon, B.; Giraldo Betancur, S.; Gallot, G. Self-referenced terahertz time-domain ATR spectroscopy of solutions. *Appl. Phys. Lett.* **2026**, *128*, 221107. [CrossRef]
17. Mazaheri, Z.; Papari, G.P.; Andreone, A. Probing the molecular dynamics of aqueous binary solutions with THz time-domain ellipsometry. *Sensors* **2023**, *23*, 2292. [CrossRef]
18. Mazaheri, Z.; Papari, G.P.; Andreone, A. Dielectric response of different alcohols in water-rich binary mixtures from THz ellipsometry. *Int. J. Mol. Sci.* **2024**, *25*, 4240. [CrossRef]
19. Fitzgerald, A.J.; Pickwell-MacPherson, E.; Wallace, V.P. Use of finite difference time domain simulations and Debye theory for modelling the terahertz reflection response of normal and tumour breast tissue. *PLoS ONE* **2014**, *9*, e99291. [CrossRef]
20. Oh, S.J.; Maeng, I.; Nam, K.S.; Yoon, Y.J.; Shim, J.-K.; Kim, J.S.; Kang, S.-G.; Jeon, M.Y.; Ryu, H.-C. Exploring the impedance-matching effect in terahertz reflection imaging of skin tissue. *Biomed. Opt. Express* **2024**, *15*, 834–842. [CrossRef]
21. Grischkowsky, D.; Keiding, S.; van Exter, M.; Fattinger, C. Far-infrared time-domain spectroscopy with terahertz beams of dielectrics and semiconductors. *J. Opt. Soc. Am. B* **1990**, *7*, 2006–2015. [CrossRef]
22. Yang, L.-H.; Maeng, I.; Lee, S.; Kim, K.; Ji, Y.B.; Bark, H.S.; Shin, H.J.; Oh, S.J. Qualitative analysis of edible oil mixture for omega-3 content using terahertz time-domain spectroscopy. *npj Sci. Food* **2025**, *9*, 140. [CrossRef]
23. Liebe, H.J.; Hufford, G.A.; Manabe, T. A model for the complex permittivity of water at frequencies below 1 THz. *Int. J. Infrared Millim. Waves* **1991**, *12*, 659–675. [CrossRef]
24. Vinh, N.Q.; Sherwin, M.S.; Allen, S.J.; George, D.K.; Rahmani, A.J.; Plaxco, K.W. High-precision gigahertz-to-terahertz spectroscopy of aqueous salt solutions as a probe of the femtosecond-to-picosecond dynamics of liquid water. *J. Chem. Phys.* **2015**, *142*, 164502. [CrossRef]
25. Haynes, W.M. (Ed.) *CRC Handbook of Chemistry and Physics*, 97th ed.; CRC Press: Boca Raton, FL, USA, 2016.
26. Shiraga, K.; Adachi, A.; Nakamura, M.; Tajima, T.; Ajito, K.; Ogawa, Y. Characterization of the hydrogen-bond network of water around sucrose and trehalose: Microwave and terahertz spectroscopic study. *J. Chem. Phys.* **2017**, *146*, 105102. [CrossRef]
27. Heugen, U.; Schwaab, G.; Bründermann, E.; Heyden, M.; Yu, X.; Leitner, D.M.; Havenith, M. Solute-induced retardation of water dynamics probed directly by terahertz spectroscopy. *Proc. Natl. Acad. Sci. USA* **2006**, *103*, 12301–12306. [CrossRef]

28. Duan, Q.; Duyn, J.H.; Gudino, N.; de Zwart, J.A.; van Gelderen, P.; Sodickson, D.K.; Brown, R. Characterization of a dielectric phantom for high-field magnetic resonance imaging applications. *Med. Phys.* **2014**, *41*, 102303. [CrossRef]
29. Captur, G.; Gatehouse, P.; Keenan, K.E.; Heslinga, F.G.; Bruehl, R.; Prothmann, M.; Graves, M.J.; Eames, R.J.; Torlasco, C.; Benedetti, G.; et al. A medical device-grade T1 and ECV phantom for global T1 mapping quality assurance—The T1 Mapping and ECV Standardization in cardiovascular magnetic resonance (T1MES) program. *J. Cardiovasc. Magn. Reson.* **2016**, *18*, 58. [CrossRef]
30. Hernandez, D.; Kim, K.-N. Correlation analysis between the complex electrical permittivity and relaxation time of tissue mimicking phantoms in 7 T MRI. *Sci. Rep.* **2022**, *12*, 15444. [CrossRef]

Disclaimer/Publisher's Note: The statements, opinions and data contained in all publications are solely those of the individual author(s) and contributor(s) and not of MDPI and/or the editor(s). MDPI and/or the editor(s) disclaim responsibility for any injury to people or property resulting from any ideas, methods, instructions or products referred to in the content.